

# COMPUTATION OF SPIRAL SPECTRA \*

PAUL WHEELER <sup>†</sup> AND DWIGHT BARKLEY <sup>‡</sup>

## Abstract.

A computational linear stability analysis of spiral waves in a reaction-diffusion equation is performed on large disks. As the disk radius  $R$  increases, eigenvalue spectra converge to the absolute spectrum predicted by Sandstede and Scheel. The convergence rate is consistent with  $1/R$ , except possibly near the edge of the spectrum. Eigenfunctions computed on large disks are compared with predicted exponential forms. Away from the edge of the absolute spectrum the agreement is excellent, while near the edge computed eigenfunctions deviate from predictions, probably due to finite-size effects. In addition to eigenvalues associated with the absolute spectrum, computations reveal point eigenvalues. The point eigenvalues and associated eigenfunctions responsible for both core and far-field breakup of spiral waves are shown.

**Key words.** spiral wave, excitable media, oscillatory media, eigenvalues, breakup.

**AMS subject classifications.**

**1. Introduction.** Rotating spiral waves are found in many chemical and biological systems and have been the subject of intense study for many years [10, 14, 16, 28]. The equations governing these systems are typically of reaction-diffusion type. Although each system is modeled in detail by specific equations — which are often very complex — generic features of the spiral waves can be understood from reaction-diffusion equations with simple nonlinearities. Figure 1.1 shows a spiral wave in a generic model reaction-diffusion system described in detail in §2. For the model parameters in figure 1.1 the spiral wave rotates with constant frequency and shape, i.e. it is a rotating wave.

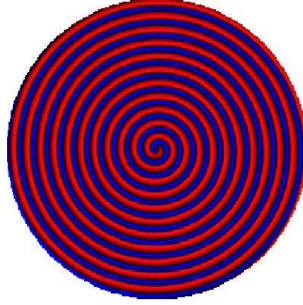


FIG. 1.1. Rotating spiral wave solution of reaction-diffusion equations described in §2. Colors indicate the level of the  $u$  field with blue used for  $u$  near zero and red used for  $u$  near 1. The wave rotates counterclockwise. The domain radius,  $R = 80$ , is approximately 10 times the spiral wavelength. Homogeneous Neumann boundary conditions, corresponding to zero chemical flux, are imposed at the domain boundary. Model parameters are  $a = 0.75$ ,  $b = 0.0006$ , and  $\epsilon = 0.0741$ .

The focus of our work is a computational study of the linear stability spectra of rotating spiral waves such as those shown in figure 1.1. To explain the motivation behind this study it is necessary to first recall the recent analysis by Sandstede and Scheel [21, 22, 23, 24] on the spectra of rotating spiral waves. Their work examines

\*Mathematics Institute, University of Warwick, Coventry, CV4 7AL

<sup>†</sup>wheeler@maths.warwick.ac.uk.

<sup>‡</sup>barkley@maths.warwick.ac.uk.

spectra on large bounded disks and on unbounded domains. The results can be summarized as follows (see figure 1.2). On large bounded disks, the linear stability spectrum consists of point eigenvalues and what is called the absolute spectrum. The absolute spectrum is not actually part of the stability spectrum. However, all but possibly a finite number of point eigenvalues converge to the absolute spectrum as the domain size tends to infinity. That is, except for finitely many eigenvalues that are created through the underlying pattern as a whole, or possibly by the boundary conditions, all eigenvalues on large bounded domains are expected to be close to the absolute spectrum. The point eigenvalues have well-defined limits as the domain size tends to infinity.

In practice the absolute spectrum must be computed numerically for any given reaction-diffusion equation, e.g. [22]. Such computations require discretization in only one space dimension and thus are relatively simple compared with computing eigenvalues of the full stability problem on a large domain, such as in figure 1.1.

For spiral waves on the unbounded plane, the linear stability spectrum consists of point eigenvalues and the essential spectrum. The essential spectrum is continuous spectrum and is determined only by the far-field waves trains of the spiral. It too is relatively easy to compute numerically in one space dimension. The point eigenvalues again depend on the underlying spiral pattern as a whole.

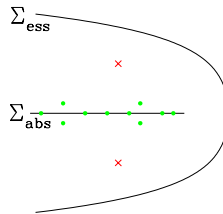


FIG. 1.2. *Illustration of spectra in the complex plane for spirals on bounded and unbounded domains.  $\Sigma_{abs}$  and  $\Sigma_{ess}$  represent the absolute and essential spectrum respectively. Points represent eigenvalues on a large bounded domain which approach  $\Sigma_{abs}$  as the domain size tends to infinity. Crosses represent the point spectrum which does not approach  $\Sigma_{abs}$  as the domain size tends to infinity.*

To see how these linear stability spectra may be relevant in practice, we show in figure 1.3 simulations of two instabilities of rotating waves on relatively large domains and the corresponding absolute and essential spectra obtained by Sandstede and Scheel [22]. In each case a rotating wave becomes unstable in a rather dramatic fashion and the spiral breaks up. Multiple spiral waves appear in each of these simulations shortly after the time shown. In figure 1.3(a) the breakup initiates in the central region of the spiral and is referred to as core breakup [3, 15, 22] whereas in figure 1.3(b) the breakup first takes place in the outer regions of the spiral and is called far-field breakup [4, 18, 22, 26, 29].

The case of far-field breakup, figure 1.3 (right), has been the subject of several past studies [1, 2, 4, 9, 18, 22, 25, 26, 29]. The breakup can be mostly understood from analysis and simulations of one-dimensional systems. While many of these studies are based on the complex Ginzburg-Landau equation, results appear to be similar for the case of reaction-diffusion equations [2, 4, 26]. The typical scenario is that as a parameter is varied the spiral first becomes convectively unstable. In a bounded domain the onset of convective instability does not generally lead to breakup because unstable modes typically propagate away from the core and are not reflected at the

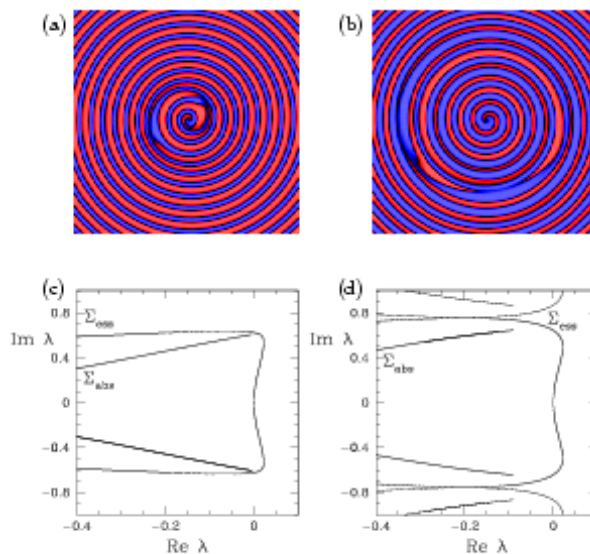


FIG. 1.3. Two examples of spiral breakup – core breakup on the left and far-field breakup on the right. The top plots show the  $u$  chemical field at about the time of breakup in numerical simulations in square geometries with homogeneous Neumann boundary conditions. Domains are of length 160 on a side. The bottom shows the absolute and essential spectrum obtained by Sandstede and Scheel for the parameter values used in the simulations. Note that these spectra repeat periodically in the imaginary direction, but this can only be seen in (d). Model parameters are: (left)  $a = 0.75$ ,  $b = 0.0006$ , and  $\epsilon = 0.0741$ , (right)  $a = 0.84$ ,  $b = -0.045$ , and  $\epsilon = 0.075$ .

boundary. As the parameter is varied further the spiral becomes absolutely unstable. Only at the absolute-instability threshold will instability surely occur in a bounded domain. Absolute instability corresponds to a growing “global mode” [25, 26], which here means an eigenfunction on the bounded domain whose eigenvalue has positive real part.

In the analysis of Sandstede and Scheel, convective instability is signaled by the crossing of the essential spectrum into the right half plane [21, 22]. Figure 1.3(d) shows that the spiral is convectively unstable. However, the spiral was already convectively unstable prior to the breakup seen in figure 1.3 and this is not the cause of breakup. The breakup is caused by an eigenvalue with positive real part and the corresponding global mode on the finite (bounded) domain. In principle such an eigenvalue could be associated with the absolute spectrum or it could be a point eigenvalue. In figure 1.3(d) the absolute spectrum is away from the imaginary axis and thus is not expected to play a direct role in the far-field breakup. Thus we expect there to be at least one positive point eigenvalue not contained in figure 1.3(d).

It is worth being clear about potentially confusing terminology. Absolute instability is not associated only with the absolute spectrum. The union of the absolute spectrum and the point spectrum determine absolute stability. If part of the absolute spectrum lies in the right half plane, then the spiral will necessarily be absolutely unstable. However, the converse is not true, since absolute instability can arise due to point eigenvalues, even if the absolute spectrum lies entirely in the left-half plane.

We should warn the reader that simulations at the stated parameters in fig-

ure 1.3(b) are very sensitive to numerical resolution. As we shall see, this is because the particular parameters considered by Sandstede and Scheel are extremely close to a transition between far-field and core breakup.

The case of core breakup, figure 1.3(left), has not been extensively analyzed, in large part because one cannot expect to capture much of the spiral core structure in one-dimensional studies. (See however [2].) Sandstede and Scheel [22] have raised the possibility that core breakup may be due to the absolute spectrum. In figure 1.3(c) it can be seen that the absolute spectrum is very near the imaginary axis, although it is entirely in the left-half plane. (The argument of Sandstede and Scheel is not simply that the absolute spectrum is close to the real axis, but the details are not important here.) The other possibility for core breakup is that the instability is again due to point eigenvalues. The essential spectrum in 1.3(c) extends into the right-half plane and so the spiral is convectively unstable.

Computing the eigenvalue spectra of spiral waves on large domains has thus become important. First and foremost, it is desirable to test the absolute spectra of Sandstede and Scheel in at least a few cases. The primary issue is whether or not eigenvalues tend to the absolute spectrum for typical domains sizes used in studies of spiral waves, e.g. domains such as those in figure 1.3. The theory is still developing and we would like to know whether absolute spectra in fact have any implications for domains of reasonable size. The other important issue which computations can address is the abundance and importance of point eigenvalues not predicted by the absolute spectrum. For example, it is desirable to know how many point eigenvalues are present within the region shown in 1.3(c)-(d), how many of these eigenvalues have positive real part, and whether or not these are associated with breakup. For these reasons we have undertaken the large-scale eigenvalue computation reported here.

Throughout this paper we shall use *point eigenvalue* to mean those eigenvalues which remain isolated as the domain radius becomes large, as contrasted with the eigenvalues associated with the absolute spectrum that approach one another as the radius becomes large. To simplify discussion we shall use *positive eigenvalue* to mean an eigenvalue, or a complex-conjugate pair of eigenvalues, with positive real part. Similarly we shall use *positive eigenfunction* to mean an eigenfunction whose corresponding eigenvalue has positive real part.

## 2. Model and Methods.

**2.1. Model.** We will consider a standard two-component reaction-diffusion model [5] given by the equations

$$(2.1a) \quad \frac{\partial u}{\partial t} = \nabla^2 u + f(u, v)$$

$$(2.1b) \quad \frac{\partial v}{\partial t} = \delta \nabla^2 v + g(u, v),$$

where

$$(2.2) \quad f(u, v) = \frac{1}{\epsilon} u(1 - u) \left( u - \frac{v + b}{a} \right)$$

There is freedom in the choice of  $g(u, v)$  and our methods will not depend on this choice. However, the results we report will be for the  $g$  proposed by Bär and Eiswirth [3]

and used by Sandstede and Scheel [22], namely

$$(2.3) \quad g(u, v) = \begin{cases} -v, & 0 \leq u < 1/3 \\ 1 - 6.75u(u-1)^2 - v, & 1/3 \leq u \leq 1 \\ 1 - v, & 1 < u \end{cases}$$

The equations are posed on a disk of radius  $R$  and with homogeneous Neumann boundary conditions at  $r = R$ :

$$\frac{\partial u}{\partial r}(R, \theta) = \frac{\partial v}{\partial r}(R, \theta) = 0,$$

where  $r, \theta$  are standard polar coordinates. For chemically reacting systems these are the most natural boundary conditions as they correspond to zero chemical flux through the boundary of the domain. Other boundary conditions could give different spiral solutions and linear stability spectra on finite domains, but we do not consider any other boundary conditions here.

The parameters of the model are kinetics parameters  $a, b$ , and  $\epsilon$ , and the diffusion coefficient  $\delta$ . If  $b > 0$  the equations model an excitable medium. In this case the homogeneous state with  $u = v = 0$  everywhere is linearly stable and finite amplitude perturbations are required to initiate waves. The perturbation threshold is set by  $b/a$ . For  $b < 0$  the equations model an oscillatory medium. In both cases  $\epsilon$  controls the time-scale ratio between the  $u$ - and  $v$ -equations. We consider  $\epsilon \ll 1$  corresponding to a fast time scale for  $u$  relative to  $v$ . We shall only report results for the case  $\delta = 0$ .  $\delta = 1$  is the other case commonly considered. As stated at the outset, these equations model generic features of spiral waves in a variety of excitable and oscillatory media.

**2.2. Computational tasks.** Consider rotating-wave solutions of (2.1) rotating at frequency  $\omega$ . We use  $(u^*, v^*)$  to denote such solutions and refer to them as steady spirals, since these are steady states when viewed in the frame of reference which is rotating with the spiral. Transforming to a system of coordinates co-rotating at frequency  $\omega$ , steady spirals obey the equations

$$(2.4a) \quad 0 = \nabla^2 u^* + \omega \frac{\partial u^*}{\partial \theta} + f(u^*, v^*)$$

$$(2.4b) \quad 0 = \omega \frac{\partial v^*}{\partial \theta} + g(u^*, v^*),$$

subject to homogeneous Neumann boundary conditions. These steady-state equations can be written in the form

$$(2.5) \quad \mathcal{F} \begin{pmatrix} u^* \\ v^* \end{pmatrix} = 0,$$

where  $\mathcal{F}$  is the nonlinear operator given by the right hand side of (2.4).

Next, given a steady spiral, we seek the leading part of its linear stability spectrum. Consider the linearized evolution equations, in the rotating frame, for infinitesimal perturbations  $(u', v')$  of the steady solution  $(u^*, v^*)$ :

$$(2.6a) \quad \frac{\partial u'}{\partial t} = \nabla^2 u' + \omega \frac{\partial u'}{\partial \theta} + f_u(u^*, v^*)u' + f_v(u^*, v^*)v'$$

$$(2.6b) \quad \frac{\partial v'}{\partial t} = \omega \frac{\partial v'}{\partial \theta} + g_u(u^*, v^*)u' + g_v(u^*, v^*)v',$$

where  $f_u, \dots, g_v$  denote the derivatives of the kinetic functions. In this frame of reference the eigenvalue problem is

$$(2.7) \quad \mathcal{L} \begin{pmatrix} \tilde{u} \\ \tilde{v} \end{pmatrix} = \lambda \begin{pmatrix} \tilde{u} \\ \tilde{v} \end{pmatrix}$$

where  $\begin{pmatrix} \tilde{u} \\ \tilde{v} \end{pmatrix}$  are eigenfunctions,  $\lambda$  are the corresponding eigenvalues, and  $\mathcal{L}$  is

$$(2.8) \quad \mathcal{L} = \begin{pmatrix} \nabla^2 + \omega \partial_\theta + f_u(u^*, v^*) & f_v(u^*, v^*) \\ g_u(u^*, v^*) & \omega \partial_\theta + g_v(u^*, v^*) \end{pmatrix}.$$

Thus our primary numerical tasks are the solution of steady state problem (2.5) and the determination of the leading eigenvalues of problem (2.7).

In addition it is necessary to perform a few simulations of the time-dependent equations (2.1), e.g., the simulations shown in figure 1.3. In the case of figure 1.3 the numerical methods are described fully elsewhere [5, 12] and will not be discussed here.

**2.3. Computational Methods.** Equations (2.5) and (2.7) are common in large-scale numerical bifurcation problems and the computational methods we employ are more or less standard [11]. For completeness we provide a basic description of our methods and stress a few points concerning implementation which are essential to the efficiency of the computations.

The fields are discretized on a regular polar grid  $(r_j, \theta_k) = (j\Delta r, k\Delta\theta)$ , where  $0 < j \leq N_r$  and  $0 \leq k < N_\theta$ , plus the center point  $(0, 0)$ . There are thus  $N_r N_\theta + 1$  grid points. The  $r$ -derivatives in the differential operators are evaluated using second-order finite differences, taking into account the boundary condition at  $r = R$ . The  $\theta$ -derivatives are evaluated spectrally using Fourier transforms. In this way (2.5) and (2.7) become

$$(2.9) \quad \mathbf{F}(\mathbf{U}^*) = 0,$$

$$(2.10) \quad \mathbf{L}\tilde{\mathbf{U}} = \lambda\tilde{\mathbf{U}}$$

where the  $\mathbf{U}$ 's are vectors of length  $N = 2(N_r N_\theta + 1)$ ,  $\mathbf{F}$  is a nonlinear function, and  $\mathbf{L}$  is an  $N \times N$  matrix.

Newton's method is used to solve steady state problem (2.9). One iteration of Newton's method is

$$(2.11) \quad \mathbf{D}\mathbf{F}(\mathbf{U}_n)\Delta\mathbf{U}_n = -\mathbf{F}(\mathbf{U}_n)$$

$$(2.12) \quad \mathbf{U}_{n+1} = \mathbf{U}_n + \Delta\mathbf{U}_n,$$

where  $\mathbf{D}\mathbf{F}(\mathbf{U}_n)$  is the linearization of  $\mathbf{F}$  about the current iterate  $\mathbf{U}_n$ . This is the same matrix as  $\mathbf{L}$  except it is evaluated at  $\mathbf{U}_n$  rather than at the steady state  $\mathbf{U}^*$ .

The work of each Newton's iteration is dominated by the work necessary to solve the  $N \times N$  linear system of equations (2.11) for the  $n^{th}$  correction  $\Delta\mathbf{U}_n$ . This can be done by a direct method if care is taken to order variables to keep the matrix bandwidth of  $\mathbf{D}\mathbf{F}$  as small as possible. Let  $u_{jk}$  and  $v_{jk}$  be values at grid point  $(r_j, \theta_k)$ . Then these are ordered in  $U_i$  such that the chemical species changes fastest with index  $i$ , followed by the angular index  $k$ , followed by the radial index  $j$ . This ordering is not that suggested by (2.8). With the ordering we use the bandwidth is

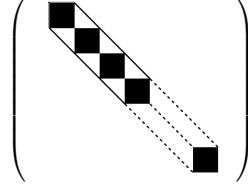


FIG. 2.1. Banded structure of matrix  $\mathbf{DF}$  or  $\mathbf{L}$ . Solid black represents full blocks of size  $2N_\theta \times 2N_\theta$  mainly due to using spectral representation of  $\theta$ -derivatives. The lines are due to the second-order finite-difference representation of  $r$ -derivatives.

approximately  $4N_\theta$ . See figure 2.1. Even for moderately large discretizations a direct method can be used to solve (2.11). For example on a grid  $N_r \times N_\theta = 600 \times 256$ ,  $N$  is approximately  $3 \times 10^5$ , while the bandwidth is only about  $10^3$ .

The only other issue concerning the steady state computations is that the frequency  $\omega$  must be found in addition to fields  $u^*$  and  $v^*$ . The existence of the additional unknown is consistent with the fact that the solution to (2.4) is not unique due to the rotational symmetry in  $\theta$ . One more algebraic equation must be added to (2.9) to remove the phase degeneracy and thus giving  $N + 1$  equations in  $N + 1$  unknowns. The constraint we add is simply to fix  $u$  as some point in the domain. While the constraint destroys the banded structure of  $\mathbf{DF}$ , a Sherman-Morrison technique [19] is used to find solutions of the augmented linear system using only the banded  $\mathbf{DF}$ .

We now describe our computations of the leading eigenvalue spectrum of  $\mathbf{L}$ . The basis of our approach is to employ a Cayley transformation to transform the eigenvalues we seek (those with largest real part) to dominant eigenvalues (of largest magnitude), and then to find iteratively dominant eigenvalues of the transformed operator. Reference [17] gives a nice review of such methods. Specifically, we consider the matrix  $\mathbf{A}$  defined by the Cayley transform

$$(2.13) \quad \mathbf{A} = (\xi \mathbf{I} + \mathbf{L})^{-1}(\eta \mathbf{I} + \mathbf{L}),$$

where  $\xi$  and  $\eta$  are real parameters and  $\mathbf{I}$  is the identity. Letting the  $\mu$  and  $\lambda$  be the eigenvalues of  $\mathbf{A}$  and  $\mathbf{L}$  respectively, we have the relation

$$(2.14) \quad \mu = \frac{\eta + \lambda}{\xi + \lambda}.$$

The parameters  $\xi$  and  $\eta$  can be adjusted so as to map the regions of interest in the  $\lambda$ -plane to large magnitude in the  $\mu$ -plane. Using the predicted absolute spectra of Sandstede and Scheel it is easy to find appropriate values of  $\xi$  and  $\eta$ . Figure 2.2 shows the effect of the Cayley transform on the absolute spectrum for one of the cases predicted by Sandstede and Scheel [22] (the other case is similar) for the values of  $\xi$  and  $\eta$  used in our computations:  $\xi = -0.4$  and  $\eta = 4.0$ . In the  $\mu$ -plane we include transforms of two periodic repeats of the absolute spectrum, one corresponding to the larger imaginary part and one to smaller imaginary part (in the  $\lambda$ -plane). These repeats are outside the region of the  $\lambda$ -plane shown. Most of the eigenvalues of  $\mathbf{L}$  lie far to the left in the  $\lambda$ -plane (outside the range of the figure). These are all mapped to near the origin by (2.13).

There is no need to form or store the matrix  $\mathbf{A}$  in order to iteratively calculate its eigenvalues. All one needs is the ability to compute  $\mathbf{A}\mathbf{U}$  for arbitrary  $\mathbf{U}$ . This

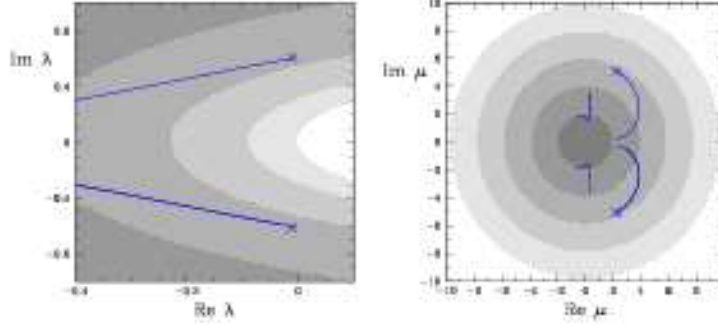


FIG. 2.2. Plot showing the effect of the Cayley transform on the absolute spectrum in 1.3(c). Left is the original and right is transformed spectrum. The right includes two periodic repeats of the absolute spectrum which are outside of the region shown on the left. Shading indicates magnitude of eigenvalues after the transformed.

is accomplished using the same basic technique as in Newton's method. Letting  $\mathbf{U}' = \mathbf{A}\mathbf{U}$  we see that  $\mathbf{U}'$  obeys

$$(2.15) \quad (\xi \mathbf{I} + \mathbf{L})\mathbf{U}' = (\eta \mathbf{I} + \mathbf{L})\mathbf{U}.$$

However,  $(\xi \mathbf{I} + \mathbf{L})$  has the same structure, in particular the same bandwidth, as  $\mathbf{L}$  and  $(\eta \mathbf{I} + \mathbf{L})$  requires mostly the same computations as evaluating  $\mathbf{F}$ . Thus we act with  $\mathbf{A}$  on  $\mathbf{U}$  by computing  $(\eta \mathbf{I} + \mathbf{L})\mathbf{U}$  to form a right-hand side and then solving a linear system with matrix  $(\xi \mathbf{I} + \mathbf{L})$ . Since this is a fixed matrix, for any given  $\mathbf{L}$ , it is factored only once for all actions of  $\mathbf{A}$ .

Dominant eigenvalues  $\mathbf{A}$  are easily found by subspace iteration [17, 27]. This method guarantees that we can obtain any required number of dominant eigenvalues to arbitrarily high precision. While Arnoldi's method generally converges faster, in practice we find that with this method all eigenvalues we require are not found with high enough precision. While there are methods, such as block Arnoldi, which could probably address this, we have used subspace iteration. From the eigenvalues  $\mu$  of  $\mathbf{A}$  we invert (2.14) to find the required eigenvalues  $\lambda$ .

**2.4. Accuracy.** We conclude this section by considering the accuracy of our computations and providing details of numerical parameters used in the results reported. The sources of error are the following:

1. Discretization error of the steady state problem, i.e. approximation of (2.5) by (2.9).
2. Residual error arising from determining the roots of (2.9) to a finite accuracy.
3. Discretization error of the eigenvalue problem, i.e. approximation of (2.7) by (2.10).
4. Residual error arising from computing eigenvalue/eigenfunction pairs (2.10) to finite accuracy.

The two residual errors are least important. We always iterate sufficiently to reduce these to negligible size. The following hold for all reported results. Solutions  $\mathbf{U}^*$  of (2.9) are found such that  $\|\mathbf{F}(\mathbf{U}^*)\| < 10^{-8}$ . Solutions of (2.10) are found such that  $\|\mathbf{L}\tilde{\mathbf{U}} - \lambda\tilde{\mathbf{U}}\| < 10^{-8}$ , where  $\|\tilde{\mathbf{U}}\| = 1$ . The norm is the vector 2-norm. The dimension  $k$  of the subspaces used in subspace iteration are:  $k = 30$  for  $R = 20$  and  $R = 40$ , and  $k = 75$  for  $R = 80$ . In all cases we stop iterations when  $\sim 0.7k$  of the



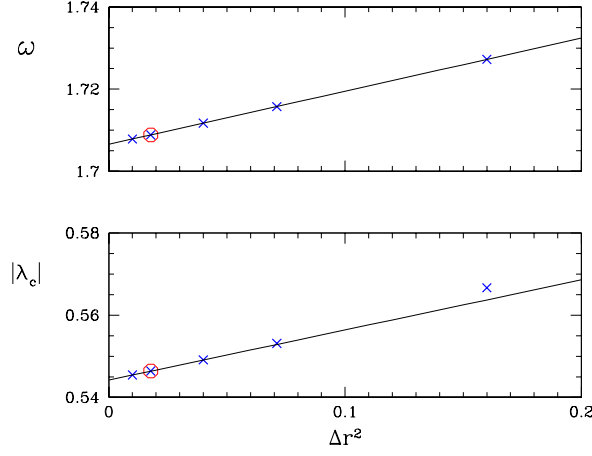


FIG. 2.3. Graphs illustrating the convergence of steady states (top) and eigenvalues (bottom) as function of grid resolution  $\Delta r^2$ , where  $\omega$  is the spiral frequency and  $\lambda_c$  is a complex eigenvalue. The domain radius is  $R = 40$ . Crosses are with  $N_\theta = 256$ . For  $\Delta r = 0.1333$  computations have been repeated with  $N_\theta = 128$  are results are shown with circles. Parameters are  $a = 0.75$ ,  $b = 0.0006$ , and  $\epsilon = 0.0741$ .

eigenvalue-eigenvector pairs have residual less than  $10^{-8}$ . In the case of  $R = 80$ , we thus obtain 53 pairs with the required residual. We initially start with a subspace generated from  $k$  random vectors, but we restart iterations from previous runs when necessary.

The discretization errors are dominated, in both the steady state and eigenvalue computations, by the second-order finite-derivative approximation to the  $r$ -derivatives in the Laplacian operator. This is expected since the  $\theta$ -derivatives are computed with spectral accuracy. Thus the dominant error in the computations depends on  $\Delta r$  in a well-understood way. Figure 2.3 shows examples of how results from steady state and eigenvalue computations scale with  $\Delta r^2$ . The domain radius is  $R = 40$ , half the maximum considered in our work. For the steady states we show the frequency  $\omega$  and for the eigenvalues we show the magnitude of  $\lambda_c$ , a complex eigenvalue associated with core breakup that will be considered in detail later in the paper. In both cases the second-order convergence is evident. We are interested only in leading eigenvalues (roughly  $10^2$  out of  $10^5$ ) all of which correspond to eigenfunctions with variation on approximately the same spatial scale (roughly the wavelength of the underlying spiral) so that the effects of the finite-difference discretization will be approximately the same for all eigenvalues we report.

Based on these plots, we use  $\Delta r = 0.1333$  for all results reported in § 3. At this value of  $\Delta r$  we have performed computations at both  $N_\theta = 128$  and  $N_\theta = 256$ . These results show clearly that  $N_\theta = 128$  gives sufficient resolution for domain radius  $R = 40$ . Therefore, for radii up to at least  $R = 80$ ,  $N_\theta = 256$  should produce smaller errors than the already small errors due to the radial discretization. In summary, for all results in § 3 we use  $\Delta r = 0.1333$  and  $N_\theta = 256$ .

### 3. Results.

**3.1. Spectra.** We begin with results for the eigenvalue spectra. Figure 3.1 shows leading eigenvalues of  $\mathbf{L}$  for the two cases considered by Sandstede and Scheel. The

spectrum corresponding to core breakup is at the top and the spectrum corresponding to far-field breakup is at the bottom. In each figure eigenvalues computed for three domain radii,  $R = 20$ ,  $R = 40$ , and  $R = 80$ , are plotted as points with dashed lines connecting eigenvalues associated with the absolute spectrum. For comparison, the absolute and essential spectra obtained by Sandstede and Scheel are shown as solid curves.

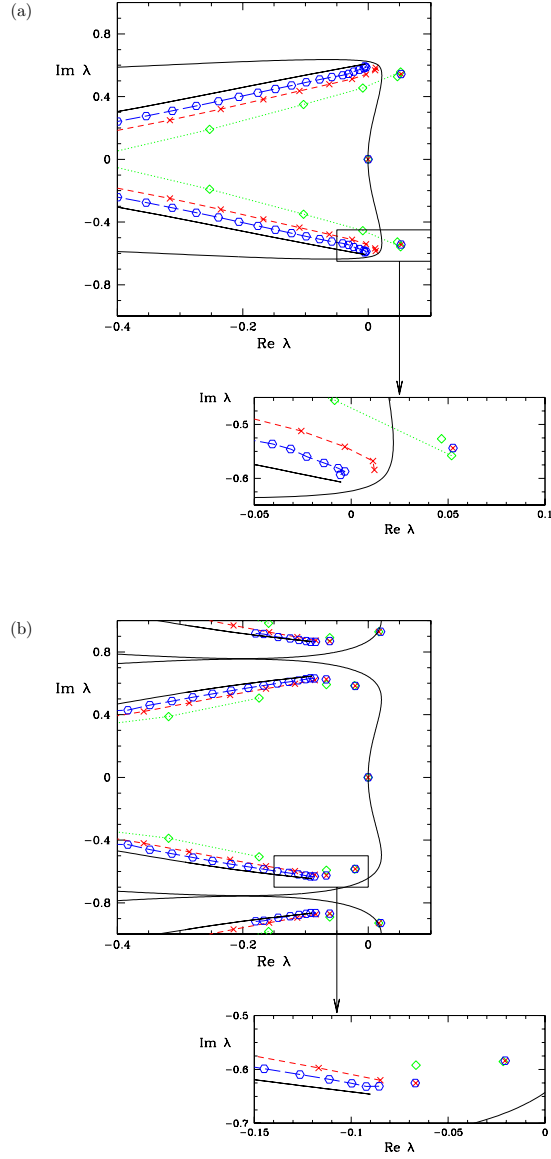


FIG. 3.1. *Eigenvalue spectra. (a) Spectrum corresponding to core breakup and (b) spectrum corresponding to far-field breakup. In each case eigenvalues are shown for three domain radii:  $R = 20$  (green diamonds),  $R = 40$  (red crosses), and  $R = 80$  (blue circles). For each radius, the eigenvalues associated with the absolute spectrum are connected with lines. Point eigenvalues are not. Parameters for (a):  $a=0.75$ ,  $b=0.0006$ ,  $\epsilon=0.0741$ ,  $\omega=1.71$ . Parameters for (b):  $a=0.84$ ,  $b=-0.045$ ,  $\epsilon=0.0751$ ,  $\omega=1.50$ .*

Before considering either case in detail, we note that the predominant feature in both is the presence of many eigenvalues which approach the predicted absolute spectra as the domain radius increases. Each doubling of  $R$  results in approximately a halving of the distance of eigenvalues to the absolute spectrum, thus supporting  $1/R$  convergence to the absolute spectrum. Furthermore the density of eigenvalues approximately doubles with each doubling of  $R$ . We return to this while considering each case in more detail. It should be noted that in the far-field case we have not obtained all eigenvalues associated with the periodic repeats of the absolute spectrum for  $R = 80$  due to the difficulties of computing these with sufficient accuracy. This results in an abrupt termination of the eigenvalue branches for  $R = 80$  at the top and bottom of figure 3.1(b).

Consider first the spectrum in figure 3.1(a) corresponding to core breakup. Within the region of the complex plane shown, there are three point eigenvalues. All other eigenvalues are associated with the absolute spectrum. Specifically, we find three eigenvalues which are insensitive to the domain radius and which are separated from the absolute spectrum. Of these, one is the zero eigenvalue arising due to rotational symmetry. There are three points indistinguishable from zero in figure 3.1(a) corresponding to the three domain radii studied. The other two point eigenvalues are a complex-conjugate pair at approximately  $0.050 \pm 0.543i$ . As we shall show in § 3.3, these eigenvalues are associated with core breakup. We will denote them by  $\lambda_c$ . (These are the eigenvalues considered in the convergence study in figure 2.3.) All other eigenvalues vary with domain radius and approach the absolute spectrum as the radius becomes large.

The enlargement in figure 3.1(a) clarifies the situation around the complex point eigenvalues. Even on the enlarged scale the point eigenvalues for  $R = 40$  and  $R = 80$  coincide. At  $R = 20$ , however, there are two nearby eigenvalues. The lower one corresponds to the absolute spectrum (indicated by the connecting dashed line) because it moves, as  $R$  is increased, toward the absolute spectrum. The other eigenvalue converges, as the  $R$  is increased, to the point eigenvalue. Note that while the edge of the eigenvalue branch associated with the absolute spectrum is near the point eigenvalue at  $R = 20$ , the branch does not approach the point eigenvalue as the domain becomes small. It is nevertheless interesting that the point eigenvalue is near the edge of the absolute spectrum. We find this throughout and return to this in the conclusion.

As already noted, the distance of eigenvalues to the absolute spectrum is approximately proportional to  $1/R$  and the density of eigenvalues is approximately proportional to  $R$ . Because we are not able to extend the computations significantly beyond the radius  $R = 80$  (already quite large) there is not enough data to draw strong conclusions about these scalings. In particular it is not clear from the data whether or not the scaling in the vicinity of the edge of the absolute spectrum is different from elsewhere. Near the edge of the spectrum the eigenvalues are more dense and closer to the absolute spectrum than elsewhere. More importantly we observe a curving and perhaps folding, at the edge of the eigenvalue branch as the radius becomes large. This would again suggest a different scaling at the spectrum's edge, but the numerical results are inconclusive.

We have focused our study on the eigenvalues within the region shown in figure 3.1(a), but we have computed some eigenvalues out side of this region. In particular our iterative technique frequently finds eigenvalues associated with the periodic repetition of the absolute spectrum in the complex plane. We have not attempted to resolve the details of the other eigenvalue branches. Also there is a complex-conjugate

pair of point eigenvalues near  $0 \pm i\omega$  due to approximate translational symmetry.

Now consider the spectrum corresponding to far-field breakup. In figure 3.1(b) we find four complex-conjugate eigenvalue pairs that we can clearly classify as point eigenvalues. One of these pairs has small positive real part and hence the spiral wave is absolutely linearly unstable, see section § 3.3. Again we observe that the point eigenvalues, except for the zero eigenvalue, appear near the edge of the absolute spectrum.

We observe approximately  $1/R$  convergence of eigenvalues to the absolute spectrum. The only apparent deviation is again at the edge of the spectrum. In this case we do not observe any curving of the eigenvalue branch seen in the enlargement in figure 3.1(a); however, we do find that the right-most point of the computed branch does not appear to approach the edge of the predicted absolute spectrum. One possibility is that this last eigenvalue is in fact a point eigenvalue very close to the edge of the absolute spectrum.

**3.2. Eigenfunctions.** In figures 3.2 and 3.3 we plot eigenfunctions for a representative selection of eigenvalues. All eigenfunctions have been obtained on a domain with  $R = 80$ , the largest we consider. Each eigenfunction is shown in two formats. In the left column eigenfunctions are visualized on the computational domain. Specifically the  $\tilde{u}$ -field of the real part of the eigenfunction is plotted with black used where the field values are near zero. The imaginary parts of the eigenfunctions are not fundamentally different. In the right column the modulus of each eigenfunction is shown as a function of radius. Specifically, we generate 16 radial sections  $|\tilde{u}(r, \theta_s)|$  where  $\theta_s = s\pi/8$  and  $s = 0, 1, \dots, 15$  and plot all 16 sections simultaneously as a function of  $r$ . The envelope of these sections gives a simple representation of the modulus of the eigenfunction as a function of  $r$ .

The technique used by Sandstede and Scheel [23] to obtain absolute and essential spectra also predict large- $r$  behavior of eigenfunctions. The main prediction is that if an eigenvalue is to the left of the essential spectrum then the corresponding eigenfunctions will be exponentially growing at large  $r$ , whereas if an eigenvalue is to the right of the essential spectrum then the corresponding eigenfunctions will be exponentially decaying at large  $r$ . In addition to the general prediction, the numerical technique employed by Sandstede and Scheel to obtain spectra for specific problems also provides the growth/decay rates for eigenfunctions. These rates [20] are indicated by the (red) lines in the right column of figures 3.2 and 3.3. For eigenfunctions corresponding to the absolute spectrum, the predicted exponential growth rates have been taken from the point on the absolute spectrum nearest to the computed eigenvalue. Only the slope of the lines is relevant. The intercept is chosen for ease of comparison with the eigenfunctions.

Consider first the eigenfunctions in figure 3.2 corresponding to the case of core breakup. The top eigenfunction is the zero mode due to rotational symmetry. This eigenfunction is given by the  $\theta$ -derivative of the underlying spiral wave and hence closely resembles the spiral. The eigenfunction neither grows nor decays at large  $r$ .

Figure 3.2(b) shows the eigenfunction corresponding to the positive complex-conjugate point eigenvalues  $\lambda_c$ . Since the eigenvalues are to the right of the essential spectrum the eigenfunction decays with  $r$ . While there is generally good agreement between the computed eigenfunction and prediction, there is some deviation from prediction that is more pronounced at larger  $r$ .

Figures 3.2(c)-(e) show three eigenfunctions associated with the absolute spectrum. The agreement between the computed eigenfunctions and predictions is ex-

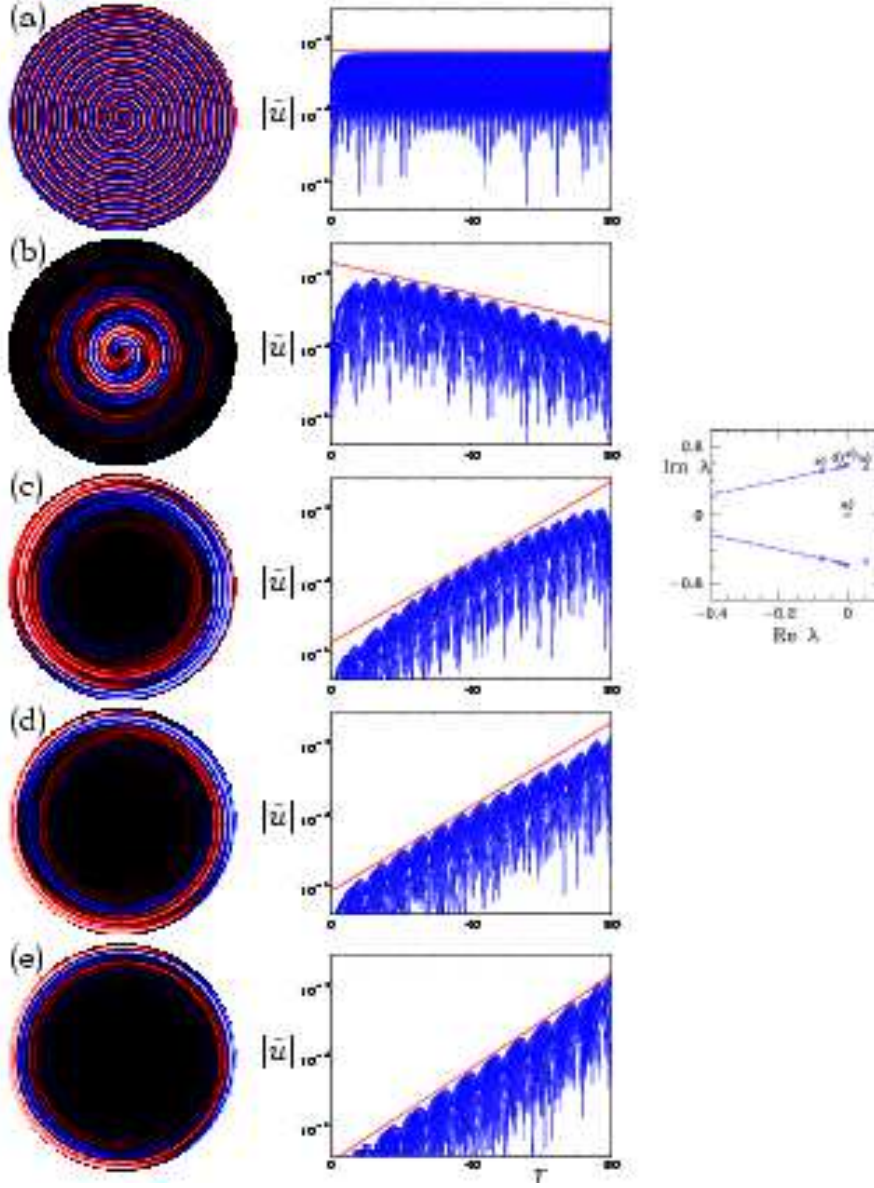


FIG. 3.2. Representative eigenfunctions for parameters corresponding to core breakup. The left column shows the real part of the each eigenfunction. The  $\tilde{u}$ -field is plotted with black used where the field is near zero. Right column shows the  $r$  dependence of  $|\tilde{u}|$  with predicted growth/decay rate also shown with lines (see text). Plot at the far right is a guide to the corresponding eigenvalues. (a) zero (rotational) eigenvalue, (b) positive eigenvalue  $\lambda_c$ , and (c), (d), (e) three representative eigenvalues associated with the absolute spectrum. Parameters as in figure 3.1(a).

tremely good away from the edge of the absolute spectrum. Near the edge the agreement is less good. In particular, eigenfunctions are not pure exponential, even at large  $r$ , and the computed eigenfunctions systematically grow more slowly than prediction. While not shown, we find that the eigenfunctions computed on smaller domains and show even slower growth as a function of  $r$ . This would suggest that the deviation

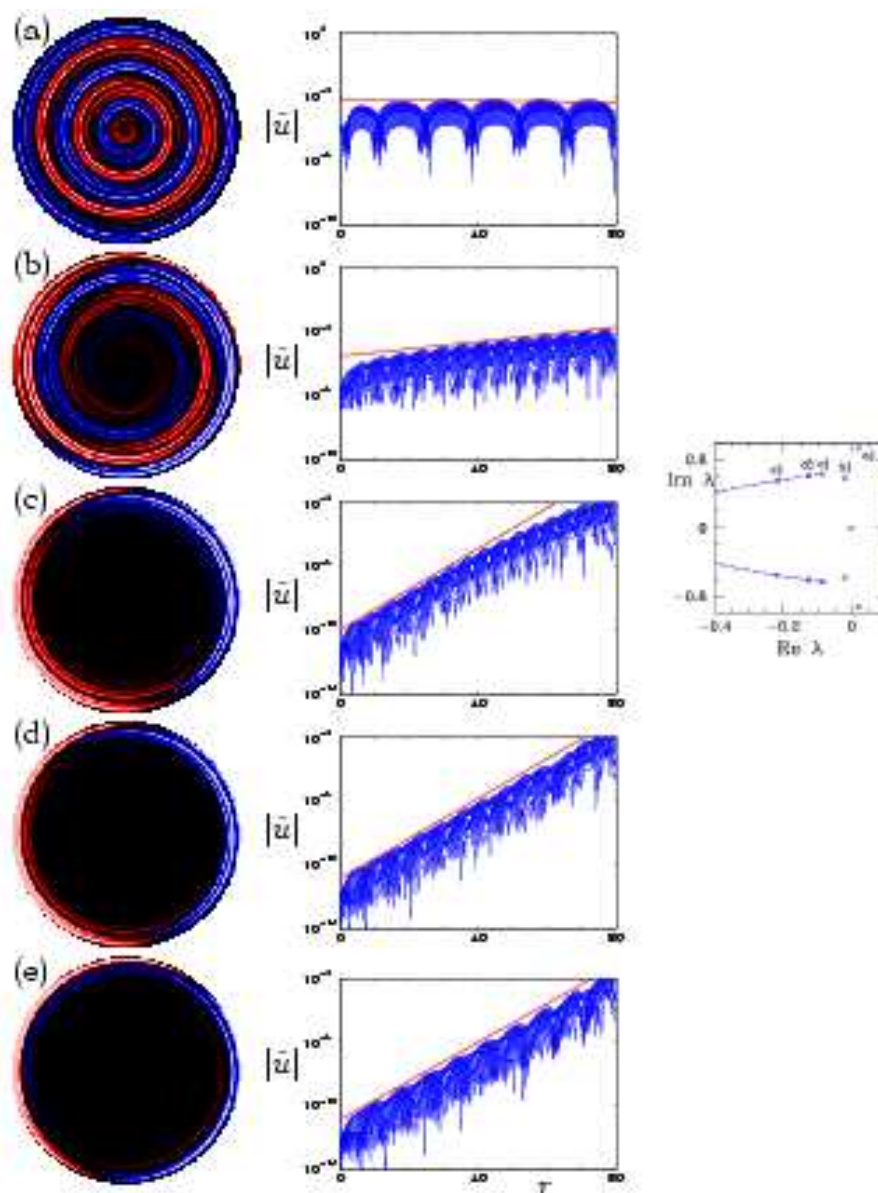


FIG. 3.3. Representative eigenfunctions for parameters corresponding to far-field breakup. Same format is used as in figure 3.2. The rotational eigenfunction is not shown. Two eigenfunctions corresponding to point eigenvalues are shown with (a) slightly positive eigenvalue and (b) slightly negative eigenvalue. (c), (d), (e) are three representative eigenvalues associated with the absolute spectrum. Parameters as in figure 3.1(b).

shown in figure 3.2(c) is due to finite domain size.

Figure 3.3 shows eigenfunctions corresponding to parameters for which far-field breakup occurs. We plot eigenfunctions corresponding to two of the complex-conjugate point eigenvalues and show three representative eigenfunction associated with the absolute spectrum. The eigenfunction corresponding to the zero eigenvalue is similar to figure 3.2(a) and is not shown.

The eigenfunctions corresponding to the point eigenvalues agree very well with prediction. The growth rate of the positive eigenfunction in figure 3.3(a) is very small since the corresponding eigenvalue is almost exactly on the essential spectrum (figure 3.1(b)). This is a fortuitous situation which illustrates nicely that the essential spectrum delimits the crossover from growth to decay of eigenfunctions. While quantitatively the agreement is very good, there is a qualitative disagreement between the computed eigenfunction and prediction. Our computed eigenfunction is growing with  $r$ , indicating that the eigenvalue is actually slightly to the left of the essential spectrum, whereas in figure 3.1(b) the eigenvalue is slightly to the right of the essential spectrum and the predicted exponent is slightly negative. The quantitative difference is very small and is likely due to a small numerical difference, e.g. a difference in the value of  $\omega$  found in our computations and that used by Sandstede and Scheel. The closeness of this eigenvalue to the essential spectrum is just by chance. If parameters are changed the eigenvalue moves away from the essential spectrum. It is because of this closeness to the eigenvalue to essential spectrum that numerical simulations at these parameter values are so sensitive to numerical resolution (as noted in § 1).

The eigenfunction in figure 3.3(b) is exponentially growing since the corresponding eigenvalue is to the left of the essential spectrum. There are no observable deviations from pure exponential growth at large  $r$  and the agreement with prediction is very good.

The three eigenfunctions associated with the absolute spectrum show the same trend as in figure 3.2. The agreement between the computed eigenfunctions and predictions is extremely good away from the edge of the absolute spectrum while near the edge eigenfunctions are not pure exponential and systematically grow more slowly than prediction. This case is even more striking than figure 3.2 for the following reasons. The growth rates in figure 3.2 are much larger than figure 3.3. (Note the scale change.) The numerical values representing the eigenfunctions span a larger range and yet the computed eigenfunctions away from the edge agree very well with predictions. There is every reason to believe that these eigenfunctions are numerically well resolved within the finite domain. Unlike the case in figure 3.2(c), here the eigenfunction closest to the edge of the spectrum, figure 3.3(c), deviates from exponential growth only at large  $r$ . There is a clear range  $r$ , up to approximately  $r = 40$ , where the eigenfunction agrees well the predicted exponential growth. This strongly suggests that the lack of agreement is due to finite-size effects. It is nevertheless interesting that these are more pronounced near the edge of the spectrum.

**3.3. Implications for breakup.** We now return to the issue of spiral breakup discussed at the outset (figure 1.3). We begin with the case of core breakup. Recall that while this was treated by Sandstede and Scheel [22, 23], they were not able to draw definite conclusions about the role of the absolute and essential spectrum in core breakup. It is already clear from the spectra in figure 3.1 that the steady spiral is linearly unstable due to the presence of positive point eigenvalues  $\lambda_c$ . Here we present additional nonlinear simulations of the breakup.

Figure 3.4 shows the time evolution from two different initial conditions each composed of the steady spiral plus a small amount of one of the computed eigenfunctions. The amplitude plotted is defined as  $A = \min_{\theta} \|U^* - R_{\theta}U\|$ , where  $R_{\theta}$  is a rotation by angle  $\theta$ . The norm is the vector 2-norm. Essentially  $A$  is the norm of the difference between the  $u$ -field of the steady spiral,  $U^*$ , and the  $u$ -field of the nonlinear solution  $U$ . The minimization over rotation is included to take into account the small drift of the nonlinear solution relative to the steady spiral.

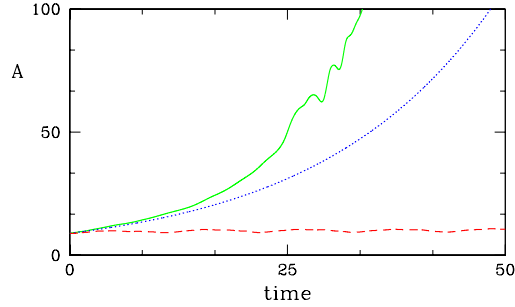


FIG. 3.4. Two time series showing the evolution starting from different perturbations of the steady spiral with parameters leading to core breakup. In one case (solid green) the perturbation is the eigenfunction corresponding to positive eigenvalue  $\lambda_c$  [(b) in figure 3.2]. In the other (dashed red) the perturbation is the eigenfunction corresponding to right-most eigenvalue associated to the absolute spectrum [(c) in figure 3.2]. The dotted blue curve shows exponential growth at rate given by  $\lambda_c$ . Parameters are as in figure 3.1(a).

Consider the evolution starting from the initial condition formed from the positive eigenfunction corresponding to  $\lambda_c$ . Accompanying visualizations are presented in figure 3.5. The dynamics is initially linear, obeying the exponential growth dictated by the real part of  $\lambda_c$ . After a short time the growth becomes nonlinear and almost immediately core breakup occurs [figure 3.5(c); time 25]. Beyond this time the amplitude  $A$  loses most of its meaning. Visualizations at much later times are shown. One of the more striking aspects of the breakup is that it occurs at  $r \simeq 20$ , not at the center of the spiral. This radius is near where the unstable eigenfunction has maximal magnitude. Visually one sees the similarity between the nonlinear breakup and the unstable eigenfunction in figure 3.5.

The initial nonlinear growth in figure 3.4 is faster than linear. This means that, at lowest order, the effect of nonlinearity on the instability is destabilizing. Such behavior occurs, for example, sufficiently close to a subcritical bifurcation, e.g. [13]. This nonlinear destabilization is consistent with the fact that small positive eigenvalues lead to the dramatic breakup of the spiral wave. If nonlinearity were stabilizing, one would expect the linear instability to saturate in a state resembling a superposition of the original spiral and a small amount of the unstable eigenmode (as occurs for example in spiral meandering [6, 7, 8]). We note that in systems such as this one the behavior can change very rapidly with parameters following a bifurcation [25, 26], and hence we are not able to conclude that the nonlinear growth follows from a subcritical bifurcation, only that at these parameter values it is destabilizing.

For completeness we have also computed the nonlinear evolution from an initial condition formed from the eigenfunction corresponding to the right-most eigenvalue of the absolute spectrum [(c) in figure 3.2]. Figure 3.4 shows the initial dynamics from this simulation. Not surprisingly  $A$  does not change much on the scale of figure 3.4 because the associated eigenvalue is very near zero. The simulation eventually leads to core breakup if run long enough. However, this is simply because the steady spiral is linearly unstable. When breakup does eventually occur, it follows the same route (e.g. same exponential growth) as for the initial condition based on the positive eigenfunction.

The conclusion is that, in this case, core breakup is due to nonlinear effects following from linear instability due to a complex-conjugate pair of point eigenvalues.



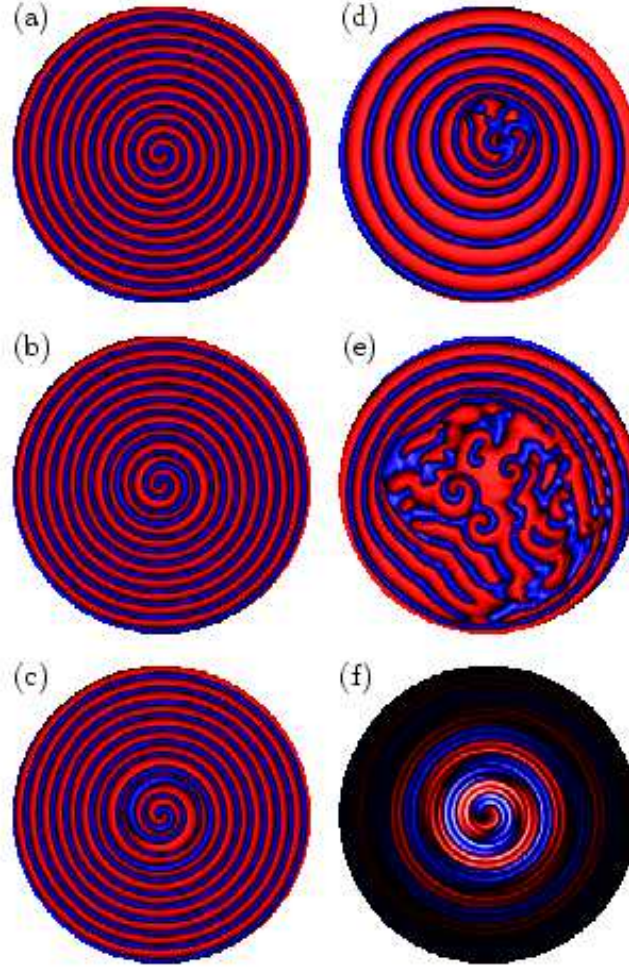


FIG. 3.5. Snapshots of evolution from the perturbed steady spiral leading to far-field breakup (solid green curve in figure 3.4). The  $u$ -field is shown with  $u \simeq 0$  blue and  $u \simeq 1$  red. (a)  $t = 0$ , (b)  $t = 20$  ( $\simeq 5$  periods), (c)  $t = 25$ , (d)  $t = 85$  ( $\simeq 23$  periods), (e)  $t = 120$  ( $\simeq 33$  periods), (f) eigenfunction. Parameters are as in figure 3.1(a).

The absolute spectrum plays no direct role in the spiral breakup.

Next we briefly consider far-field breakup. We have directly computed the eigenfunction associated with absolute instability causing far-field breakup, figure 3.3(a). The leading eigenfunction shows exactly the long wavelength modulation of the steady spiral expected for this instability [1, 4, 9, 18, 26, 29]. Figures 3.6 and 3.7 show the dynamics following from the steady spiral perturbed by the unstable eigenfunction. The dynamics are initially that of exponential growth with the expected growth rate. The growth becomes nonlinear and long-wavelength modulation of spiral becomes visible (time 80 in figure 3.7). Shortly thereafter the spiral breaks near the domain boundary. At these parameter values the eigenfunction grows weakly with radius, as seen in figure 3.3(a), and for this reason one would expect a preference for breakup near the domain boundary. However, in this case the qualitative character of eigen-

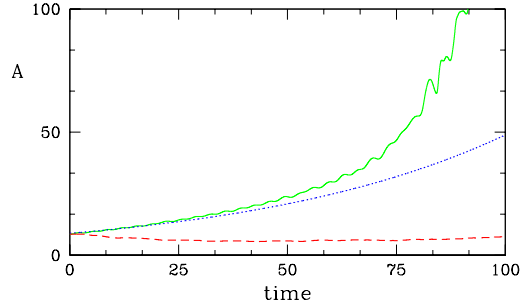


FIG. 3.6. Two time series showing the evolution starting from different perturbations of the steady spiral with parameters leading to far-field breakup. In one case (solid green) the perturbation is the eigenfunction corresponding to positive eigenvalue [(a) in figure 3.3]. In the other (dashed red) the perturbation is the eigenfunction corresponding to the weakly stable point eigenvalue [(b) in figure 3.3]. The dotted blue curve shows exponential growth at rate given by the positive eigenvalue. Parameters are as in figure 3.1(b).

function depends sensitively on parameters and for slightly different parameters the eigenfunction may decay weakly with radius.

The far-field case is similar to the core breakup case in most other respects. The nonlinear growth in figure 3.6 is faster than linear. No other eigenvalues appear to play a direct role in the far-field breakup. Figure 3.6 shows the evolution from an initial condition formed from the eigenfunction corresponding to the complex-conjugate point eigenvalues near the imaginary axis [(b) in figure 3.3].

**4. Conclusions.** In this paper we have examined in detail the linear stability spectra and associated eigenfunctions for spiral waves in large domains. Everywhere, except possibly near the edges of the absolute spectra, numerically computed eigenvalues and eigenfunctions agree extremely well with the results of Sandstede and Scheel. Our results answer the question posed at the outset. Absolute spectra can be relevant and predictive for typical domain sizes used in studies of spiral waves. Even in domains containing only a few spiral wavelengths (the case  $R = 20$ ) eigenvalues show signs of the absolute spectrum - they lie along curves located roughly in the correct part of the complex plane. For domains containing five spiral wavelengths or more ( $R \gtrsim 40$ ) eigenvalues lie quite close to the absolute spectra. Of course these results are for the particular equations and parameters studied here and absolute spectra will not necessarily be such good predictors for domains of these sizes in other systems. Nevertheless, in at least two cases, one with excitable dynamics and one with oscillatory dynamics, absolute spectra are predictive.

The computed eigenvalues support convergence to the absolute spectrum inversely with the domain radius, at least away from the edge of the absolute spectrum. In most cases eigenfunctions agree with the exponential forms deduced by Sandstede and Scheel. This is even the case for point eigenvalues not associated with the absolute spectrum. Near the edges of the absolute spectrum, however, eigenfunctions do not exhibit exponential growth at large radius, even in the largest domains we have considered. While results suggest that this is due to finite-size effects, more work is necessary to understand the behavior of eigenvalues and eigenfunction near the edges of the spectrum.

We have computed the positive point eigenvalues giving rise to both core and

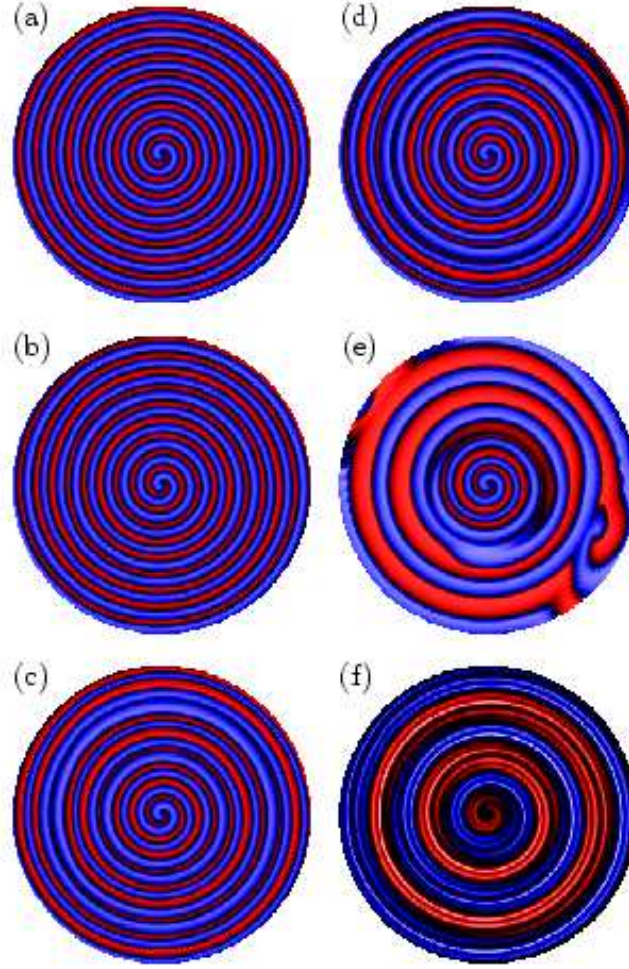


FIG. 3.7. Snapshots of evolution from the perturbed steady spiral leading to far-field breakup (solid green curve in figure 3.6). The  $u$ -field is shown. (a)  $t = 0$ , (b)  $t = 50$  ( $\simeq 12$  periods), (c)  $t = 80$  ( $\simeq 19$  periods), (d)  $t = 85$ , (e)  $t = 120$  ( $\simeq 29$  periods), (f) eigenfunction. Parameters are as in figure 3.1(b).

far-field breakup of spiral waves. The essential difference between the two cases is the form of the eigenfunctions. For core breakup the eigenfunction has a maximum not far from the core of the spiral and decays at large radius. For far-field breakup the eigenfunction grows with radius. Moreover, the far-field eigenfunction shows long-wavelength modulation known to precede far-field breakup. Nonlinearity also plays a role in breakup and we have presented nonlinear simulations showing the destabilizing effects of nonlinearity in each case.

The most intriguing aspect of this work is that all point eigenvalues we have found appear near edges of the absolute spectra. This may be a coincidence, but it would not seem so from figure 3.1. We leave this as an open problem.

**Acknowledgments.** We are very grateful to Bjorn Sandstede and Arnd Scheel for helpful discussions and for kindly providing data used for many of the comparisons presented.

## REFERENCES

- [1] I. ARANSON, L. ARANSON, L. KRAMER, AND A. WEBER, *Stability limits of spirals and traveling waves in nonequilibrium media*, Phys. Rev. A, 46 (1992), pp. R2992–R2995.
- [2] M. BÄR AND L. BRUSCH, *Breakup of spiral waves caused by radial dynamics: Eckhaus and finite wavenumber instabilities*, New J. Phys., 6 (2004), pp. 1–22.
- [3] M. BÄR AND M. EISWIRTH, *Turbulence due to spiral breakup in a continuous excitable medium*, Phys. Rev. E, 48 (1993), pp. R1635–R1637.
- [4] M. BÄR AND M. OR-GUIL, *Alternative scenarios of spiral breakup in a reaction-diffusion model with excitable and oscillatory dynamics*, Phys. Rev. Lett., 82 (1999), pp. 1160–1163.
- [5] D. BARKLEY, *A model for fast computer-simulation of waves in excitable media*, Physica D, 49 (1991), pp. 61–70.
- [6] ———, *Linear-stability analysis of rotating spiral waves in excitable media*, Phys. Rev. Lett., 68 (1992), pp. 2090–2093.
- [7] ———, *Euclidean symmetry and the dynamics of rotating spiral waves*, Phys. Rev. Lett., 72 (1994), pp. 164–167.
- [8] ———, *Spiral meandering*, in Chemical Waves and Patterns, R. Kapral and K. Showalter, eds., Kluwer, 1995, pp. 163–190.
- [9] L. BRUSCH, A. TORCINI, AND M. BÄR, *Doppler effect of nonlinear waves and superspirals in oscillatory media*, Phys. Rev. Lett., 91 (2003), p. 108302.
- [10] M. C. CROSS AND P. C. HOHENBERG, *Pattern-formation outside of equilibrium*, Rev. Mod. Phys., 65 (1993), pp. 851–112.
- [11] E. DOEDEL AND L. S. TUCKERMAN, eds., *Numerical Methods for Bifurcation Problems and Large-Scale Dynamical Systems*, IMA Volumes in Mathematics and its Applications, vol. 119, Springer, New York, 2000.
- [12] M. DOWLE, R. M. MANTEL, AND D. BARKLEY, *Fast simulations of waves in three-dimensional excitable media*, Int. J. Bifur. Chaos, 7 (1997), pp. 2529–2546.
- [13] R. D. HENDERSON AND D. BARKLEY, *Secondary instability in the wake of a circular cylinder*, Phys. Fluids, 8 (1996), pp. 1683–1685.
- [14] R. KAPRAL AND K. SHOWALTER, eds., *Chemical Waves and Patterns*, Kluwer, 1995.
- [15] A. KARMA, *Spiral breakup in model equations of action potential propagation in cardiac tissue*, Phys. Rev. Lett., 71 (1993), p. 1103.
- [16] J. KEENER AND J. SNEYD, *Mathematical Physiology*, Springer, New York, 1998.
- [17] K. MEERBERGEN AND D. ROOSE, *Matrix transformations for computing rightmost eigenvalues of large sparse non-symmetric eigenvalue problems*, IMA Journal of Numerical Analysis, 16 (1996), pp. 297–346.
- [18] Q. OUYANG AND J. M. FLESSELLES, *Transition from spirals to defect turbulence driven by a convective instability*, Nature, 379 (1996), pp. 143–146.
- [19] W. PRESS, B. FLANNERY, S. TEUKOLSKY, AND W. VETTERLING, *Numerical recipes in C*, Cambridge University Press, 1992.
- [20] B. SANDSTEDE, *Private Communication*, , 2004.
- [21] B. SANDSTEDE AND A. SCHEEL, *Absolute and convective instabilities of waves on unbounded and large bounded domains*, Physica D, 145 (2000), pp. 233–277.
- [22] ———, *Absolute versus convective instability of spiral waves*, Phys. Rev. E, 62 (2000), pp. 7708–7714.
- [23] ———, *Superspiral structures of meandering and drifting spiral waves*, Phys. Rev. Lett., 86 (2001), pp. 171–174.
- [24] ———, *Stability, and instability, of spiral waves*, , (unpublished).
- [25] S. TOBIAS, M. PROCTOR, AND E. KNOBLOCH, *Convective and absolute instabilities of fluid flows in finite geometry*, Physica D, 113 (1998), pp. 43–72.
- [26] S. M. TOBIAS AND E. KNOBLOCH, *Breakup of Spiral Waves into Chemical Turbulence*, Phys. Rev. Lett., 80 (1998), pp. 4811–4814.
- [27] L. N. TREFETHEN AND D. BAU, *Numerical Linear Algebra*, SIAM, Philadelphia, 1997.
- [28] A. T. WINFREE, *When time breaks down*, Princeton Univ. Press, Princeton, 1987.
- [29] L. ZHOU AND Q. OUYANG, *Experimental Studies on Long-Wavelength Instability and Spiral Breakup in a Reaction-Diffusion System*, Phys. Rev. Lett., 85 (2000), pp. 1650–1653.